OPEN ACCESS

University of BRISTOL

Groh, R., & Weaver, P. M. (2015). Mass Optimisation of Variable Angle Tow, Variable Thickness Panels with Static Failure and Buckling Constraints. In 56th AIAA/ASCE/AHS/ASC Structures, Structural Dynamics, and Materials Conference. American Institute of Aeronautics and Astronautics Inc.. 10.2514/6.2015-0452

Peer reviewed version

Link to published version (if available):
10.2514/6.2015-0452

Link to publication record in Explore Bristol Research
PDF-document

University of Bristol - Explore Bristol Research

General rights

This document is made available in accordance with publisher policies. Please cite only the published version using the reference above. Full terms of use are available:
http://www.bristol.ac.uk/pure/about/ebr-terms.html

Take down policy

Explore Bristol Research is a digital archive and the intention is that deposited content should not be removed. However, if you believe that this version of the work breaches copyright law please contact open-access@bristol.ac.uk and include the following information in your message:

• Your contact details
• Bibliographic details for the item, including a URL
• An outline of the nature of the complaint

On receipt of your message the Open Access Team will immediately investigate your claim, make an initial judgement of the validity of the claim and, where appropriate, withdraw the item in question from public view.

Mass Optimization of Variable Angle Tow, Variable Thickness Panels with Static Failure and Buckling Constraints

RMJ Groh [*] and PM Weaver [†]

Advanced Composites Centre for Innovation and Science,

Queen's Building, University Walk, Bristol, BS8 1TR, UK

By taking advantage of curved fiber paths, Variable Angle Tow (VAT) laminates increase the design space for tailoring the structural behavior of thin-walled aerospace structures. In recent years, advancements in Automated Fiber Placement (AFP) and Continuous Tow Shearing (CTS) have facilitated the manufacture of these laminates. The CTS technique holds the advantage of reducing many of the manufacturing defects characteristic of the AFP process such as fiber wrinkling, tow gaps and tow overlaps, while also allowing for tighter steering radii. On the other hand, the CTS process features added complexity due to the coupling of fiber steering angle with tow thickness. In this study, a minimum-mass design of a typical aircraft wing panel under end-compression subject to pre-defined manufacturing, static failure and buckling load constraints is sought. The geometric effects of the asymmetric thickness distribution of the CTS panel on the critical buckling loads, postbuckling paths and static failure behavior are captured for the first time. A hybrid optimization scheme that couples a genetic algorithm with a pattern-search algorithm is used to define a VAT laminate that reduces the mass of both square and rectangular aircraft panels by 31% compared to a baseline straight fiber design. The optimization of the fiber paths is driven by two distinct requirements, namely local and global stiffness tailoring that influence the buckling performance and static strength, respectively. Finally, the initial postbuckling behavior of the optimized designs is investigated using Koiter's perturbation approach, which reveals that postbuckling stability should be considered when optimising VAT panels manufactured by the CTS technique.

Nomenclature

VAT	Variable Angle Tow
CTS	Continuous Tow Shearing
AFP	Advanced Fiber Placement
GA	Genetic Algorithm
TWFC	Tsai-Wu Failure Criterion
M	Mass
ΔM	Percentage mass reduction
a	Length of panel
b	Width of panel
θ^k	Local fiber orientation of layer k
ϕ^k	Rotation of fiber path with respect to global x-axis of layer k
T_0^k	Fiber orientation at ply center with respect to ϕ^k
T_1^k	Fiber orientation at ply edges with respect to ϕ^k
α^k	Shearing angle of fiber path in layer k
t^k	Local thickness of layer k
t_0^k	Pristine, unsheared thickness of layer k

---

*PhD Student, Department of Aerospace Engineering, University of Bristol, UK

†Professor in Lightweight Structures, Department of Aerospace Engineering, University of Bristol, UK

ρ	Density of material
N	Number of layers in laminate
$\boldsymbol{A}, \boldsymbol{D}$	Reduced in-plane and flexural stiffness matrix of classical laminate analysis
$\boldsymbol{N}, \boldsymbol{M}$	Membrane and bending moments per unit width of classical laminate analysis
A_1, A_2	Lame parameters
$\boldsymbol{u}$	Three dimensional displacement field $(u \quad v \quad w)$
$\boldsymbol{\epsilon}$	Total strain vector $(\epsilon_x \quad \epsilon_y \quad \epsilon_{xy})$
$\boldsymbol{e}$	Linear strain vector $(e_x \quad e_y \quad e_{xy})$
$\boldsymbol{E}$	Nonlinear strain vector $(E_x \quad E_y \quad E_{xy})$
$\boldsymbol{\kappa}$	Linear curvature vector $(\kappa_x \quad \kappa_y \quad \kappa_{xy})$
R	Local radius of curvature of neutral surface
$\boldsymbol{u}_i$	The ith displacement field of the power series solution to the bifurcation problem
p	Perturbation parameter and power series variable taken as w_1^{max}/t_0 in the present paper
λ_c	Critical eigenvalue of the buckling problem
λ_1, λ_2	Slope and curvature path coefficients of the postbuckling equilibrium path
K_{pb}	Linearized postbuckling stiffness
R_{tw}	Reserve factor for static failure based on the Tsai-Wu failure criterion

I.   Introduction

The idea of tailoring the structural performance of composite laminates by spatially varying the pointwise fiber orientations over the planform has been explored since the early 1970's.[1] For example, the work by Hyer & Lee[2] and Hyer & Charette[3] showed that such variable angle tow (VAT) laminates can improve the stress concentrations around holes by arranging the fibers in the direction of critical load paths.

In recent years the use of fiber reinforced composites in primary aircraft structures has led to increased interest in VAT technology. Numerous works have shown that tailoring the in-plane stiffness of a plate allows prebuckling stresses to be re-distributed to supported regions, thereby improving the buckling behavior.[4–7] Specifically, Gurdal et al.[5] have shown that varying the stiffness of the panel perpendicular to the direction of applied end compression results in greater improvements than stiffness variations in the direction of loading. In this manner, van den Brink et al.[8] improved the buckling performance of a composite fuselage window section by 12% compared to an equivalent straight fiber laminate,[8] whereas Alhajahmad et al.[9] alleviated the pressure pillowing of fuselage sections. Furthermore, Coburn et al.[10] investigated the concept of using VAT technology to design blade-stiffened wing panels with greater critical buckling loads and lower Poisson's ratio mismatch between base plate and stiffener foot. Recent results show that VAT plates with linear fiber variations can be designed to exhibit smaller stiffness reductions in the postbuckling regime than their straight fiber counterparts.[11] Furthermore, the optimum fiber orientations for increasing the buckling load are similar to those for minimising the transverse displacement in the postbuckling regime.[12]

To date, the primary technology for manufacturing VAT laminates is Automated Fiber Placement (AFP), a manufacturing process originally developed in the 1980's to automate lamination of straight fiber laminates. AFP uses a robotic fiber placement head that deposits multiple pre-impregnated tows of "slit-tape" allowing cutting, clamping and restarting of every single tow. While the robotic head follows a specific fiber path, tows are heated shortly before deposition and then compacted onto the substrate using a special roller. Due to the high fidelity of current robot technology AFP machines can provide high productivity and handle complex geometries.[13] However, in AFP steering is accomplished by bending the tows in-plane which leads to local fiber buckling on the inside radii of the curved tow and thus limits the steering radius of curvature.[14] Furthermore, if individual tows are placed next to each other by shifting the reference path along a specific direction, tow gaps and overlaps are inevitably required to cover the whole surface. Fayazbakhsh et al.[15] showed that the presence of gaps may reduce the optimized buckling load by up to 15% compared to pristine designs. To overcome the drawbacks of AFP machines the Continuous Tow Shearing (CTS) technique was developed to use shear deformation to steer fibers at the point of application.[16] This technique not only allows much tighter radii of curvature but tow gaps and overlaps are also avoided by tesselating tows on the substrate. In recent characterization work, Kim et al.[17] showed that CTS can produce impregnation quality similar to commerical pre-preg. Most importantly for structural applications, CTS produces VAT laminates with fiber paths curved more than ten times those available from conventional AFP machines without producing tow cuts or resin pockets.

One feature of CTS is that in order to maintain the volume fraction of fiber, the thickness of a tow inherently increases as it is sheared. The relation between unsheared tow thickness t_0^k and sheared tow thickness t^k of a layer k is

$$t^k = \frac{t_0^k}{\cos \alpha^k} = t_0^k \sec \alpha^k \tag{1}$$

where α^k is the shearing angle of the tow at the point of application. Consequently, the thickness of a ply may locally increase by a factor of three if the fiber tow is sheared through an angle of $70°$. As the laminate is cured on a tool plate, one side of the laminate remains flat whereas the other resembles a curved panel as depicted in Figure 1. The effects of this asymmetric profile in terms of local three-dimensional stress fields, buckling loads and postbuckling behavior is relatively unexplored.

In practical applications composite laminates are typically modeled as thin plates and shells because the thickness dimension t is an order of magnitude smaller than representative in-plane dimensions. This feature allows the problem to be reduced from a three-dimensional (3D) to a two-dimensional (2D) one coincident with a chosen reference surface. Due to the differences in topology between the top and bottom surfaces (see Figure 1) the profile of the chosen reference plane is not immediately obvious. It is clear from fundamental mechanics that the structure bends about its neutral plane, and is therefore appropriate as the reference plane in an equivalent single layer model of buckling and postbuckling under uniform end-compression or dead load. For a symmetrically laminated CTS panel the neutral plane is coincident with the geometrical centroid of the cross-section, as shown by the dashed curve in Figure 1. In previous work on symmetrically laminated VAT panels two different modeling approaches, one including and the other disregarding the curvature of the reference plane, were compared against 3D finite element (FE) solutions.[18] The results showed that for moderate fiber variations up to $45°$ the plate formulation agrees well with the 3D FE solution but that for higher degrees of tow steering the shell formulation is required for accurate buckling load predictions.

The aim of the present work is to provide further evidence that a shell formulation is required to accurately model the buckling and postbuckling behavior of CTS panels. Based on this insight, a minimum-mass optimization strategy for a typical aircraft wing panel under end-compression is performed subject to pre-defined manufacturing, static failure and minimum buckling load constraints. Most previous optimization work has focused on designing AFP manufactured variable stiffness panels using FE techniques. Setoodeh et al.[19] performed an optimization study in FE where the fiber orientation angles at the nodes are treated as design variables. A generalized reciprocal approximation was used that allowed the maximization of buckling load to be carried out at each node separately. The authors noted that due to the non-convexity of the problem the optimization results depend on the starting points. Ijsselmuiden et al.[20] addressed the problem of non-convexity by using lamination parameters as the design variables and demonstrated buckling load improvements in excess of 100% compared to the optimum constant stiffness designs. In a follow-up study, van Campen et al.[21] proposed a methodology for converting the optimal lamination parameter distribution into realistic fiber paths, taking into account constraints on in-plane fiber path curvature. Nik et al.[22] performed a multi-objective optimization of in-plane stiffness and buckling load for a laminated plate with curvilinear fiber paths by using a surrogate-based genetic algorithm. The researchers found that varying the fiber direction perpendicular to the direction of compression can improve the buckling load of a flat plate with unconstrained lateral edges by 116% compared to a quasi-isotropic laminate. Later, it was shown that gaps and overlaps degrade and improve the structural performance along the in-plane stiffness/buckling load Pareto front, respectively.[23]

Only a small number of optimization studies have implemented numerical solution techniques that reduce the computational effort compared to FE solvers. Wu et al.[6] used a genetic algorithm (GA) in combination with the Rayleigh-Ritz solution technique. The novelty of Wu's approach is the use of Lagrange polynomials to define the fiber paths based on a finite number of grid points, allowing any order of nonlinear fiber variation to be represented. Liu & Butler[24] performed a gradient-based mass minimization strategy with buckling load constraints for variable stiffness panels specifically manufactured using the CTS technique. As a result, the study includes the effect of thickness variation on the structural behavior. However, the researchers based their structural model on a symmetric thickness variation thereby neglecting the effect of the curved neutral surface.

To the authors' knowledge, no optimization work on CTS panels exists that combines the influence of thickness variation and the geometric effect of the curved neutral surface in a minimum mass study subject to both static failure and stability constraints. The aim of this paper is to fill this gap by finding an optimum variable stiffness design for a CTS-manufactured wing panel. The rest of the paper is structured
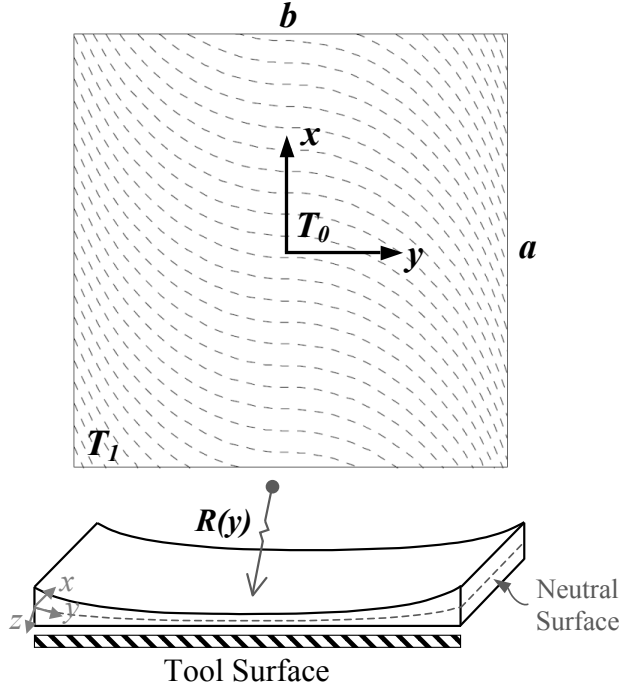
Figure 1: CTS manufactured $90\langle 0|70\rangle$ layer with the reference path shifted in the x-direction for tesselation. The schematic shows fiber orientations and thickness variation. The 3D structure is compressed onto an equivalent single layer described by a curved reference surface of varying radius of curvature.

as follows. Section II outlines the theory of modeling the variable curvature neutral surface of the CTS panel and the corresponding thin-shell, large deflection governing equations. These nonlinear differential equations are solved asymptotically using an implementation of Koiter's perturbation approach outlined in Section II.B. The importance of incorporating the geometric effect of the curved neutral surface is outlined in Section III and the results of the optimization study are shown in Section IV. Finally, conclusions are drawn in Section V.

II.   Theory

II.A.   Modeling the Variable Thickness Cross-Section

Linear fiber variations in one direction only, i.e prismatic variations, can conveniently be defined using the notation of Gurdal & Olmedo,[4]

$$\theta = \phi\langle T_0|T_1\rangle. \tag{2}$$

Here ϕ denotes the rotation of the fiber path with respect to the global x-axis, and angles T_0 and T_1 are the fiber directions at the ply center and at a characteristic length d from the center, respectively, with respect to the global rotation ϕ. Thus the angle ϕ also represents the direction of fiber variation. To tesselate tows on the substrate using the CTS technique, the fiber trajectories are shifted perpendicular to ϕ. For example, a $90\langle 0|70\rangle$ VAT layer is drawn schematically in Figure 1. Both the fiber orientation and thickness profile vary in the global y-direction and are constant in the x-direction.

Various studies have shown that fiber variations perpendicular to applied end-compression provide greater improvements in buckling load than fiber variations along the load direction.[5–7] This occurs due to the favorable redistribution of prebuckling stresses towards supported edges that do not buckle. Referring to Figure 1 with axial compression applied in the x-direction, such an effect is achieved with fiber variations in the y-direction, requiring $\phi^k = 90°$. In the case of CTS panels with $\phi^k = 90°$ the load-redistribution effect towards the edges is further increased due to the thickness build-up at the panel edges.

Throughout the paper, the analysis is constrained to symmetric laminations of CTS layers such that the in-plane/out-of-plane coupling matrix $\boldsymbol{B}(x,y)$ is assumed to be zero everywhere. As a result, the neutral

axis of the cross-section must be coincident with the geometric centroid. Using the relationship between shearing angle and thickness of Eq. (1), a parametric equation for the curved neutral surface of a laminate comprised of N CTS plies with $\phi^k = 90°$, in terms of cartesian co-ordinates x and y reads

$$\vec{r}(x,y) = x\vec{i} + y\vec{j} + \frac{1}{2}\left\{ t(x,y) - \min_{y \in [y_\wedge, y_\vee]} t(x,y) \right\} \vec{k}$$

$$\vec{r}(x,y) = x\vec{i} + y\vec{j} + \frac{1}{2}\left\{ \sum_{k=1}^N t_0^k \sec \alpha^k(y) - \min_{y \in [y_\wedge, y_\vee]} \sum_{k=1}^N t_0^k \sec \alpha^k(y) \right\} \vec{k} \tag{3}$$

where $\vec{i}$, $\vec{j}$ and $\vec{k}$ are unit vectors in the standard orthonormal basis of $\mathbb{R}^3$, and $y_\wedge$ and $y_\vee$ are the minimum and maximum bounds of the y-coordinate, respectively. The pristine ply thickness of layer k is given by t_0^k, and α^k is the sheared fiber angle of layer k at location (x,y). To prevent gaps and overlaps by tesselation of tow paths, the unsheared fiber direction must align with the direction of fiber variation such that $\alpha^k(x,y) = \theta^k(x,y) - \phi^k$. For the present study with fiber variations in the y-direction $\alpha^k(x,y) = \theta^k(x,y) - 90°$.

The neutral surface in Eq. (3) describes a cylindrical curve with variable radius of curvature. To define the kinematic relations between strain and displacement the Lamé parameters need to be known. These are

$$A_1 = |\vec{r}_{,x}| = |\vec{i}| = 1 \tag{4}$$

$$A_2 = |\vec{r}_{,y}| = \left| \vec{j} + \frac{1}{2}\sum_{k=1}^N t_0^k \alpha_{,y}^k \sec \alpha^k \tan \alpha^k \cdot \vec{k} \right| = \sqrt{1 + \left(\frac{1}{2}\sum_{k=1}^N t_0^k \alpha_{,y}^k \sec \alpha^k \tan \alpha^k \right)^2} \tag{5}$$

where the comma denotes differentiation.

To model the buckling and postbuckling behavior of the CTS panel a generalized form of Donnell's nonlinear shell equations derived by Amabili[25] are used. The classical Kirchhoff assumptions of mid-plane normals remaining normal and unextended, and plane sections remaining plane are invoked. Thus, transverse shear strains and transverse normal strains are deemed negligible compared to their in-plane counterparts. Furthermore, Lagrangian linear kinematics with von Kármán nonlinear strains are employed. Therefore,

$$\boldsymbol{\epsilon} = \boldsymbol{e} + \boldsymbol{E} + z\boldsymbol{\kappa} \tag{6}$$

where $\boldsymbol{e}$ and $\boldsymbol{E}$ are the linear and nonlinear stretching strains, respectively,

$$e_x = \frac{\partial u}{\partial x}, \quad e_y = \frac{1}{A_2}\frac{\partial v}{\partial y} + \frac{w}{R}, \quad e_{xy} = \frac{\partial v}{\partial x} + \frac{1}{A_2}\frac{\partial u}{\partial y} \tag{8a-c}$$

$$E_x = \frac{1}{2}\left(\frac{\partial w}{\partial x} \right)^2, \quad E_y = \frac{1}{2}\left(\frac{1}{A_2}\frac{\partial w}{\partial y} \right)^2, \quad E_{xy} = \frac{1}{A_2}\frac{\partial w}{\partial x}\frac{\partial w}{\partial y} \tag{8d-f}$$

and $\boldsymbol{\kappa}$ are the linear bending curvatures,

$$\kappa_x = -\frac{\partial^2 w}{\partial x^2} \tag{8a}$$

$$\kappa_y = \frac{1}{R}\frac{\partial u}{\partial x} + \frac{1}{RA_2}\frac{\partial v}{\partial y} + \frac{A_{2,y}}{(A_2)^3}\frac{\partial w}{\partial y} - \frac{1}{(A_2)^2}\frac{\partial^2 w}{\partial y^2} \tag{8b}$$

$$\kappa_{xy} = -\frac{1}{RA_2}\frac{\partial u}{\partial y} + \frac{1}{R}\frac{\partial v}{\partial x} - \frac{2}{A_2}\frac{\partial^2 w}{\partial x \partial y}. \tag{8c}$$

where $u(x,y)$, $v(x,y)$ and $w(x,y)$ are the unknown deformation variables of the curved reference surface with respect to the local xyz-coordinate system shown in Figure 1.

The governing field equations in terms of the functional unknowns u, v and w are derived using the principle of virtual displacements. The principle of virtual displacements states that a body is in equilibrium if the virtual work done by the equilibrium forces, when the body is perturbed by a virtual amount $\delta \boldsymbol{u}$ from the true configuration $\boldsymbol{u}$, is zero. Thus, for the two-dimensional shell under Kirchhoff assumptions considered here,

$$\delta \Pi = \int_V \left(\sigma_x \delta \epsilon_x + \sigma_y \delta \epsilon_y + \tau_{xy} \delta \gamma_{xy} \right) \mathrm{d}V - \int_{S_2} \left(\hat{\sigma}_n \delta u_n + \hat{\tau}_{ns} \delta u_s + \hat{\tau}_{nz} \delta w \right) \mathrm{d}S_2 = 0 \tag{9}$$

where S_2 is the boundary surface on which the stresses $\hat{\sigma}_n$, $\hat{\tau}_{ns}$ and $\hat{\tau}_{nz}$ are prescribed, and n and s are the normal and tangential directions to the boundary, respectively. Substituting the strains of Eq. (6) into Eq. (9), integrating the stresses in the z-direction and performing the calculus of variations results in a set of Euler-Lagrange equations that define the governing field and boundary equations of the theory. The governing field equations are

$$\delta u : N_{x,x} + \frac{1}{R}M_{y,x} + \left(\frac{N_{xy}}{A_2}\right)_{,y} - \left(\frac{M_{xy}}{RA_2}\right)_{,y} = 0 \tag{10a}$$

$$\delta v : \left(\frac{N_y}{A_2}\right)_{,y} + \left(\frac{M_y}{RA_2}\right)_{,y} + N_{xy,x} + \frac{1}{R}M_{xy,x} = 0 \tag{10b}$$

$$\delta w : M_{x,xx} + 2\left(\frac{M_{xy,x}}{A_2}\right)_{,y} + \left(\frac{M_y}{(A_2)^2}\right)_{,yy} - \frac{N_y}{R} + \left(M_y\frac{A_{2,y}}{(A_2)^3}\right)_{,y} + \underline{(N_xw_{,x})_{,x} + \frac{1}{A_2}(N_{xy}w_{,y})_{,x} +}$$

$$\underline{\left(\frac{N_{xy}}{A_2}w_{,x}\right)_{,y} + \left(\frac{N_y}{(A_2)^2}w_{,y}\right)_{,y}} = 0 \tag{10c}$$

where the nonlinear parts of the governing equations have been underlined in Eq. (10c). These represent the transverse components of the membrane forces that arise once the panel has buckled. The membrane forces and bending moments per unit width in Eq. (10) are defined by

$$\boldsymbol{N} = \begin{pmatrix} N_x & N_y & N_{xy} \end{pmatrix}^T = \int \begin{pmatrix} \sigma_x & \sigma_y & \sigma_{xy} \end{pmatrix}^T \mathrm{d}z = \boldsymbol{A}(x,y) \cdot (\boldsymbol{e} + \boldsymbol{E}) \tag{11a}$$

$$\boldsymbol{M} = \begin{pmatrix} M_x & M_y & M_{xy} \end{pmatrix}^T = \int z \begin{pmatrix} \sigma_x & \sigma_y & \sigma_{xy} \end{pmatrix}^T \mathrm{d}z = \boldsymbol{D}(x,y) \cdot \boldsymbol{\kappa} \tag{11b}$$

where $\boldsymbol{A}$ and $\boldsymbol{D}$ are the membrane and bending stiffness matrixes of the Classical Laminate Analysis. Note that due to the variable stiffness design of the panel both $\boldsymbol{A}$ and $\boldsymbol{D}$ are functions of location (x,y).

Finally, the essential and natural boundary conditions are given by

$$\delta u = 0 \quad \text{or} \quad \left[N_x + \frac{M_y}{R}\right]n_x + \left[\frac{N_{xy}}{A_2} - \frac{M_{xy}}{RA_2}\right]n_y = \hat{N}_x n_x + \hat{N}_{xy}n_y \tag{12a}$$

$$\delta v = 0 \quad \text{or} \quad \left[\frac{N_y}{A_2} + \frac{M_y}{RA_2}\right]n_y + \left[N_{xy} + \frac{M_{xy}}{R}\right]n_x = \hat{N}_{xy}n_x + \hat{N}_y n_y \tag{12b}$$

$$\delta w = 0 \quad \text{or} \quad \left[N_x w_{,x} + M_{x,x} + \frac{N_{xy}}{A_2}w_{,y} + \left(\frac{M_{xy}}{A_2}\right)_{,y}\right]n_x + \left[\frac{N_y}{(A_2)^2}w_{,y} + M_y\frac{A_{2,y}}{(A_2)^3} + \left(\frac{M_y}{(A_2)^2}\right)_{,y}\right.$$

$$\left. + \frac{N_{xy}}{A_2}w_{,x} + \left(\frac{M_{xy}}{A_2}\right)_{,x}\right]n_y = \hat{Q}_x n_x + \hat{Q}_y n_y \tag{12c}$$

$$\delta w_{,x} = 0 \quad \text{or} \quad M_x n_x + \frac{M_{xy}}{A_2}n_y = \hat{M}_x n_x + \hat{M}_{xy}n_y \tag{12d}$$

$$\delta w_{,y} = 0 \quad \text{or} \quad \frac{M_y}{(A_2)^2}n_y + \frac{M_{xy}}{A_2}n_x = \hat{M}_y n_y + \hat{M}_{xy}n_x. \tag{12e}$$

Here, the directional terms are defined by $n_x = \cos\upsilon$ and $n_y = \sin\upsilon$ where υ is the angle between the normal to the boundary and the global x-axis.

II.B. Koiter's Perturbation Approach

A large number of studies regarding the solution of von Kármán's nonlinear differential equations for the postbuckling behavior of plates using either energy methods[26–28] or Fourier-series expansions[29, 30] were published in the early to mid-part of the 20th century. Today, nonlinear structural analysis no longer presents the same extent of difficulty due to the sophistication of finite element based incremental-iterative procedures, such as Newton-Raphson and Riks algorithms. Despite the advances in computer hardware repeated solutions of large nonlinear systems that arise in the finite element method remain computationally expensive.[31] Although these methods have their merits for anaylising "deep" postbuckling behavior they are computationally prohibitive for optimization problems.

In the present work, the postbuckling behavior is studied using Koiter's perturbation approach.[32] The advantage of this asymptotic technique is that the nonlinear behavior past a certain bifurcation point is approximated using a power series in terms of an aribitrary small parameter. As a result, the prebuckling, buckling and initial postbuckling behaviors are captured in just three solution steps compared to multiple iterations required in incremental algorithms. Koiter's approach was applied by Stein[33] for rectangular isotropic plates, Chandra & Raju[34] for symmetrically laminated orthotropic plates, and was extended in an optimization framework by Wu et al.[35] Furthermore, Koiter's perturbation technique lends itself to robust implementation in numerical solution techniques such as the Finite Element Method (FEM)[36] and the Differential Quadrature Method (DQM).[37] Recently, Koiter's perturbation scheme was coupled with a Newton-Raphson iterative solver in order to combine the merits of both asymptotic and path-following techniques, thereby allowing efficient modeling of nonlinear prebuckling paths and limit-point buckling.[38]

In Koiter's approach the nonlinear differential equations (10) are reduced to an infinite set of linear differential equations. This is achieved by expanding the unknown functional fields $(u\ v\ w)$ in a power series of an arbitrary perturbation parameter p and a linear scalar λ of the external load,

$$\boldsymbol{u}(\lambda, p) = \begin{pmatrix} u & v & w \end{pmatrix}^T = \boldsymbol{u}_0(\lambda) + p\boldsymbol{u}_1 + p^2\boldsymbol{u}_2 + \ldots \tag{13}$$

where T represents the transpose of the vector. In this work the perturbation parameter is chosen to be the normalized buckling amplitude w_1^{max}/t_0, where w_1^{max} is the transverse buckling mode amplitude w_1, and t_0 is the total unsheared thickness of the laminate.

The first three sets of linear differential equations pertain to the prebuckling, buckling and initial post-buckling solutions, respectively. These three sets of equations are expanded in the Appendix and are solved successively for $\boldsymbol{u}_0$, $\boldsymbol{u}_1$ and $\boldsymbol{u}_2$. To linearize the prebuckling solution $\boldsymbol{u}_0$, small rotations are assumed $(w_{0,x} = w_{0,y} = 0)$ which is a valid assumption for shallow curved panels under uniaxial compression with lateral edges free to expand, i.e. no biaxial load state. The second set of equations is a linear eigenvalue problem that yields the buckling eigenvalues λ_c and eigenmodes $\boldsymbol{u}_1$. The initial postbuckling solution $\boldsymbol{u}_2$ corresponding to a particular buckling mode $\boldsymbol{u}_1$ is calculated by solving the third set of differential equations.

After the three displacement fields have been found it is possible to compute the change in load factor λ for a given change in the perturbation parameter p. Thus, expanding the load factor in a power series in terms of p gives

$$\lambda = \lambda_c + p\lambda_1 + p^2\lambda_2 + \ldots \tag{14}$$

where λ_1 and λ_2 are the slope and curvature of the equilibrium path, respectively. These path parameters can be found using the following integral expressions[39]

$$\lambda_c = \frac{1}{D} \int_A \left(\boldsymbol{N}_1^T \cdot \boldsymbol{e}_1 + \boldsymbol{M}_1^T \cdot \boldsymbol{\kappa}_1 \right) \mathrm{d}A \tag{15a}$$

$$\lambda_1 = \frac{3}{2D} \int_A \left(\boldsymbol{N}_1^T \cdot \boldsymbol{E}_{11} \right) \mathrm{d}A \tag{15b}$$

$$\lambda_2 = \frac{1}{D} \int_A \left(\boldsymbol{N}_2^T \cdot \boldsymbol{E}_{11} + 2\boldsymbol{N}_1^T \cdot \boldsymbol{E}_{12} + \lambda_1 \boldsymbol{N}_0^T \cdot \boldsymbol{E}_{12} \right) \mathrm{d}A \tag{15c}$$

$$D = - \int_A \boldsymbol{N}_0^T \cdot \boldsymbol{E}_{11} \mathrm{d}A \tag{15d}$$

where

$$E_{ij} = \left[w_{i,x}w_{j,x} \quad \frac{w_{i,y}w_{j,y}}{(A_2)^2} \quad \frac{w_{i,x}w_{j,y} + w_{j,x}w_{i,y}}{A_2} \right]^T$$

and N_i and M_i are the membrane resultants and bending moments, respectively, of the ith perturbation step corresponding to p^i. The parameters λ_1 and λ_2 represent the slope and curvature of the postbuckling path, respectively, for $p > 0$. Thus, the stability of the structure can be ascertained directly from these path parameters. A non-zero value of the slope parameter λ_1 indicates asymmetry about the bifurcation point and means the structure exhibits a load drop or a displacement jump at the bifurcation point for controlled end-shortening and dead load, respectively. Furthermore, a non-zero value of λ_1 makes the structure sensitive to initial imperfections. The structure is stable if $\lambda_2 > 0$ and unstable if $\lambda_2 < 0$ because these signs indicate a rising and falling load-displacement path past the bifurcation point, respectively.

The perturbed form of the governing equations (10) are solved in the strong form using an implementation of the Differential Quadrature method (DQM) in MATLAB. DQM is a numerical technique for solving differential boundary value problems developed in the 1970s by Bellmann et al.[40] Since then DQM has been shown to give robust and efficient solutions to many problems in structural mechanics.[41] Details on implementing Koiter's perturbation approach in DQM are presented by White et al.[37]

II.C.   Tsai-Wu Failure Criterion

To assess the likelihood of static failure of the VAT panels in the compressive prebuckling regime the stress-based Tsai-Wu failure criterion (TWFC)[42] is implemented. The TWFC is chosen because it accounts for interaction between different stress components and provides good failure predictions within the current engineering requirements.[43] Furthermore, the TWFC has been identified as one of the five best performing failure criterion assessed in the recent World-Wide Failure Exercise and is recommended for uni-directional lamina under combined loading.[44]

For a state of plane-stress in the through-thickness direction the failure index I_F according to the orthotropic TWFC is

$$I_F = F_1\sigma_{11} + F_2\sigma_{22} + 2F_{12}\sigma_{11}\sigma_{22} + F_{11}\sigma_{11}^2 + F_{22}\sigma_{22}^2 + F_{66}\sigma_{12}^2 \tag{16}$$

where σ_{11} and σ_{22} are the longitudinal and transverse stress components to the fiber direction, respectively, and σ_{12} is the in-plane shear stress. The coefficients F_{ij} of the orthotropic TWFC in Eq. (16) are given by

$$F_1 = \frac{1}{X_t} - \frac{1}{X_c}, \quad F_2 = \frac{1}{Y_t} - \frac{1}{Y_c}, \quad F_{12} = f^*\sqrt{F_{11}F_{22}}$$
$$F_{11} = \frac{1}{X_t X_c}, \quad F_{22} = \frac{1}{Y_t Y_c}, \quad F_{66} = \frac{1}{S^2} \tag{17}$$

where X_t, X_c, Y_t and Y_c are experimentally determined material failure strengths in uniaxial tension t and compression c in the longitudinal X and transverse Y directions to the fibers, respectively. The in-plane shear strength is given by S and all five experimental strengths in Eq. (17) take positive signs. The magnitude of the normalized interaction term f^* is difficult to ascertain experimentally and a value of $f^* = -0.5$ is chosen here based on suggested ranges in the literature.[43]

The TWFC is applied to each ply in the laminate separately, bearing in mind that the stresses within each VAT ply are functions of location such that $I_F = I_F(x,y)$. Thus, to prevent local failure over the whole laminate domain the failure indexes related to each ply is required to satisfy

$$\max_{k\in[1,N]} I_F^k(x,y) < 1 \tag{18}$$

for a total of N plies within the VAT laminate.

A more intuitive way of expressing the likelihood of failure is to use a factor of safety f, which is the factor by which all laminate stress components need to be multiplied by to instigate failure. The factor of safety is calculated by combining Eqs. (16) and (18) and assuming that all stresses scale linearly with f,

$$\left(F_{11}\sigma_{11}^2 + F_{22}\sigma_{22}^2 + F_{66}\sigma_{12}^2 + 2F_{12}\sigma_{11}\sigma_{22}\right)f^2 + \left(F_1\sigma_{11} + F_2\sigma_{22}\right)f - 1 = 0$$

$$\therefore f = \frac{-\left(F_1\sigma_{11} + F_2\sigma_{22}\right) + \sqrt{\left|\left(F_1\sigma_{11} + F_2\sigma_{22}\right)^2 + 4\left(F_{11}\sigma_{11}^2 + F_{22}\sigma_{22}^2 + F_{66}\sigma_{12}^2 + 2F_{12}\sigma_{11}\sigma_{22}\right)\right|}}{2\left(F_{11}\sigma_{11}^2 + F_{22}\sigma_{22}^2 + F_{66}\sigma_{12}^2 + 2F_{12}\sigma_{11}\sigma_{22}\right)}. \tag{19}$$

By definition, a ply is safe from failing if $f > 1.0$. In the present work the factor of safety is expressed in terms of the reserve factor $R_{tw} = 1/f$, whereby R_{tw} expresses how close each ply is to failing. Thus, to prevent local failure in any ply k the reserve factor needs to satisfy

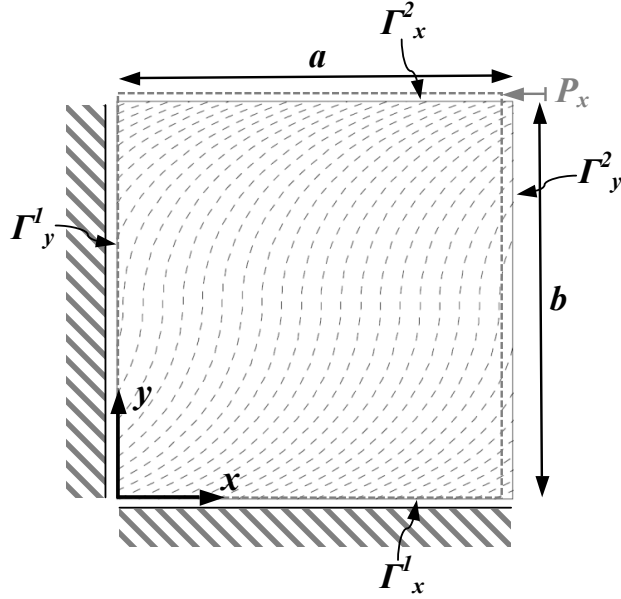$$\max_{k\in[1,N]} R_{tw}^k(x,y) < 1. \tag{20}$$

Figure 2: Schematic of CTS panel with boundary conditions and applied load case.

III.   Model Validation

III.A.   Problem Definition

To ascertain the accuracy of the presented model a number of rectangular VAT panels with length a and width b as shown in Figure 2 are analysed under various different boundary conditions summarized in Table 1. In all analysed cases, the four edges Γ_x^1, Γ_x^2, Γ_y^1 and Γ_y^2 are supported against transverse displacement, are free to slide, and are forced to remain straight - the latter condition is not generally guaranteed due to the variable stiffness nature of the laminate. Furthermore, edges Γ_x^1 and Γ_y^1 are constrained from expanding normal to their boundaries and a compressive force $P_x = -250$ kN is applied along edge Γ_y^2. With the width of the panel fixed at $b = 0.25$ m, the applied load case corresponds to an edge load of 1 kN/mm, which is a typical value for aircraft wing panels. In terms of the functional field $\boldsymbol{u}$ these general boundary conditions are

$$
\begin{aligned}
\text{Straight Edges:} \quad & u_{,y}(0,y) = u_{,y}(a,y) = v_{,x}(x,0) = v_{,x}(x,b) = 0 \\
\text{Transverse Support:} \quad & w(x,0) = w(x,b) = w(0,y) = w(a,y) = 0 \\
\text{Free to slide:} \quad & N_{xy}(x,0) = N_{xy}(x,b) = N_{xy}(0,y) = N_{xy}(a,y) = 0 \\
\Gamma_x^1 \text{ and } \Gamma_y^1 \text{ constrained:} \quad & u(0,y) = v(x,0) = 0 \\
\text{Applied Force:} \quad & P_x = \int_0^b N_x(a,y)\mathrm{d}y = -250 \text{ kN}
\end{aligned}
\tag{21}
$$

The general boundary conditions in Eq. (21) are combined with different rotational boundary conditions and a boundary condition on in-plane y-direction displacement v for edge Γ_x^2, as summarized in Table 1. The shorthand notation used herein to refer to specific boundary conditions is given in the first column.

III.B.   Effect of Curved Neutral Surface

To investigate the influence of the shell effect with increasing steering angle, an eight-ply $[90 \pm \langle 0|T_1\rangle]_{2s}$ CTS panel was analysed for different values of edge angle T_1. The analysis was based on a square panel with dimensions $a = b = 0.25$ m and three distinct boundary conditions BC_{C4}^f, BC_{C4}^c and BC_{S2C2}^f. The laminate stiffness properties were assumed to be two-dimensional orthotropic and are representative of IM7 8552 with $E_{11} = 163$ GPa, $E_{22} = 12$ GPa, $G_{12} = 5$ GPa, $v_{12} = 0.3$ and ply thickness of 0.125 mm.

The DQ form of the governing equations was implemented in MATLAB in two different manners. The first, denoted by *DQ Shell*, includes the geometric curvature of the neutral surface and the second, denoted

Table 1: Different boundary conditions and corresponding shorthand notation.

| Notation | Rotational Condition | | | | In-plane Condition |
	on Γ_x^1	on Γ_x^2	on Γ_y^1	on Γ_y^2	on Γ_x^2
BC_{C4}^f	Clamped	Clamped	Clamped	Clamped	free
BC_{C4}^c	Clamped	Clamped	Clamped	Clamped	constrained
BC_{S2C2}^f	Pinned	Pinned	Clamped	Clamped	free
BC_{S4}^f	Pinned	Pinned	Pinned	Pinned	free

by *DQ Plate*, uses the flat plate equations of classical Kirchhoff theory, thereby neglecting the geometric curvature of the neutral surface. Both the *DQ Shell* and *DQ Plate* models are compared against a 3D FEM analysis of the actual asymmetric CTS panel in the commercial software package Abaqus. Furthermore, 2D FE analogs to the analytical DQ formulations named *2D FE Shell* and *2D FE Plate* with curved and flat reference surfaces, respectively, were created in Abaqus. In all models, the mesh density was increased until the results converged to within 0.1%. In the 3D FEM, results converged using a mesh with one C3D8R element per ply and 100 elements in both planform directions. The 2D FEM models implemented 100 S4R elements in both planform dimensions for converged solutions. In all FE models, the first critical buckling loads and corresponding buckling modes were found using a linear eigenvalue analysis. To examine the initial postbuckling behavior the first buckling mode was then scaled by 10^{-5} and applied as an imperfection onto the nodal co-ordinates in a second geometrically nonlinear Riks analysis.

Figure 3 compares the accuracy of the *DQ Shell*, *2D FE Shell*, *DQ Plate* and *2D FE Plate* linear buckling load predictions against the 3D FEM solution with changing edge angle T_1 for boundary conditions BC_{C4}^f and BC_{S2C2}^f. In all cases the analytical DQ and the 2D FE solutions are closely matched. It is clear that for small amounts of fiber steering $T_1 < 45°$, and thus small amounts of neutral axis curvature, the *DQ Plate* and *2D FE Plate* results maintain good correlation with the 3D FEM results. As the edge angle T_1 increases the *DQ Plate* and *2D FE Plate* solutions become increasingly more inaccurate resulting in a maximum error of 3.4% compared to 1.3% for the *DQ Shell* and *2D FE Shell* solutions.

Figure 4a shows the same comparison of buckling load accuracy for boundary condition BC_{C4}^c. This plot does not include the results of the *DQ Shell* formulation because the lateral constraint on edges Γ_x^1 and Γ_x^2 in boundary condition BC_{C4}^c creates a bi-axial load state with an associated nonlinear prebuckling solution due to the geometric curvature of the neutral surface. This nonlinear behavior on the fundamental path can not be captured in the present *DQ Shell* formulation due to the assumption of small prebuckling rotations ($w_{0,x} \approx 0$ and $w_{0,y} \approx 0$). Figure 4a shows a discrepancy of up to 14% between the *2D FE Plate* solution and the 3D FEM solution, whereas the *2D FE Shell* solution remains accurate with nominal errors. Furthermore, Figure 4b shows the prebuckling and postbuckling load/end-shortening equilibrium paths for two edge angles $T_1 = 45°$ and $T_1 = 70°$. In both cases the *2D FE Plate* solution cannot capture the nonlinear prebuckling path due to the assumption of a flat reference surface that prevents coupling between the in-plane displacements u, v and the transverse displacement w in the prebuckling regime.

Figure 5 compares the load versus end-shortening curves of the *DQ Shell* and 3D FEM solutions in the prebuckling and initial postbuckling regimes for boundary conditions BC_{C4}^f and BC_{S2C2}^f. In all cases the initial postbuckling equilibrium paths are well correlated. In some instances the analytical *DQ Shell* solution loses accuracy in the deeper postbuckling regime but this may be remedied by extending the asymptotic series in Eq. (13) to include higher order terms in p. Overall, the results presented indicate that the curvature of the neutral surface needs to be taken account of to accurately capture the structural behavior of CTS panels.
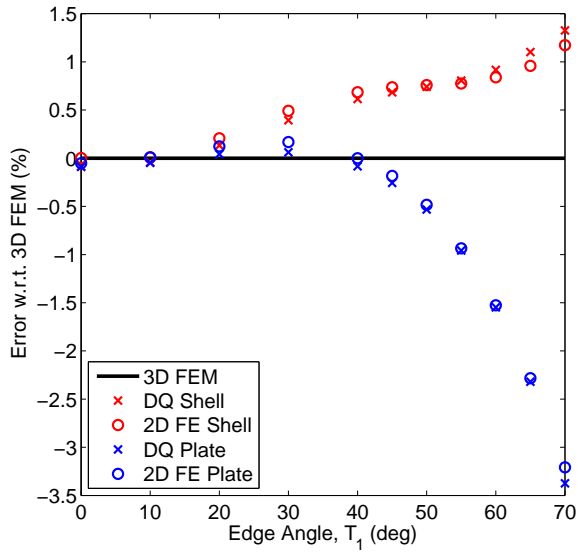
IV. Optimization

IV.A. Optimization Scheme

The *DQ Shell* model introduced above is used to optimize the fiber paths of a square ($a = b = 0.25$ m) and a rectangular ($a = 0.75$ m, $b = 0.25$ m) CTS panel with fiber paths steered in the y-direction, i.e. $\phi^k = 90°$, subject to boundary conditions BC_{S4}^f and compressive force $P_x = -250$ kN as described in Section III.A.
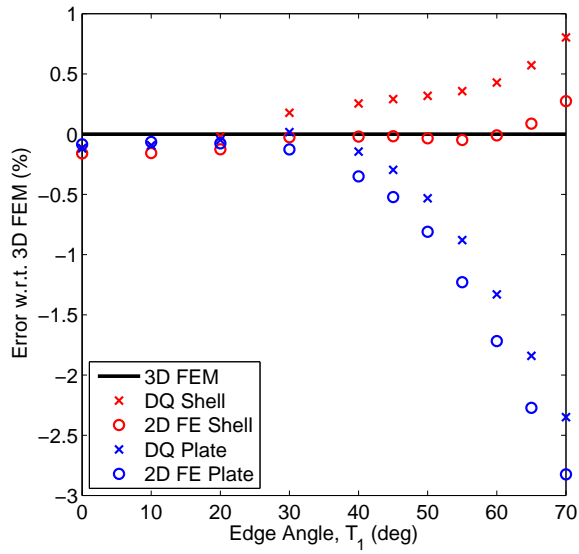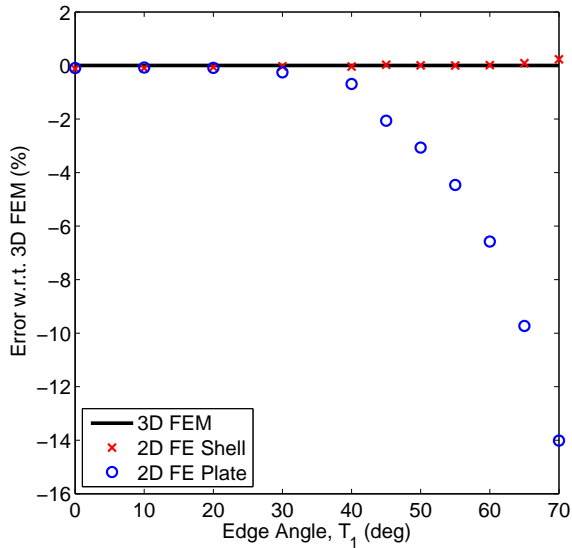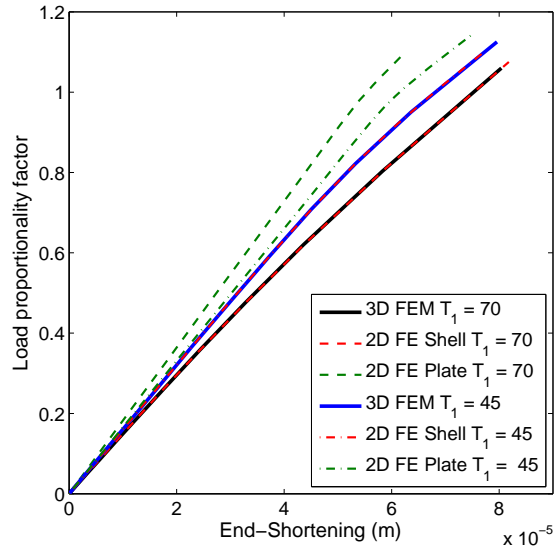
(a) BC_{C4}^f

(b) BC_{S2C2}^f

Figure 3: Comparison of DQ Plate, DQ Shell, 2D FE Plate, 2D FE Shell and 3D FEM predictions of linear buckling load versus edge angle T_1 of a $[90 \pm \langle 0|T_1 \rangle]_{2s}$ CTS laminate for two separate boundary conditions.
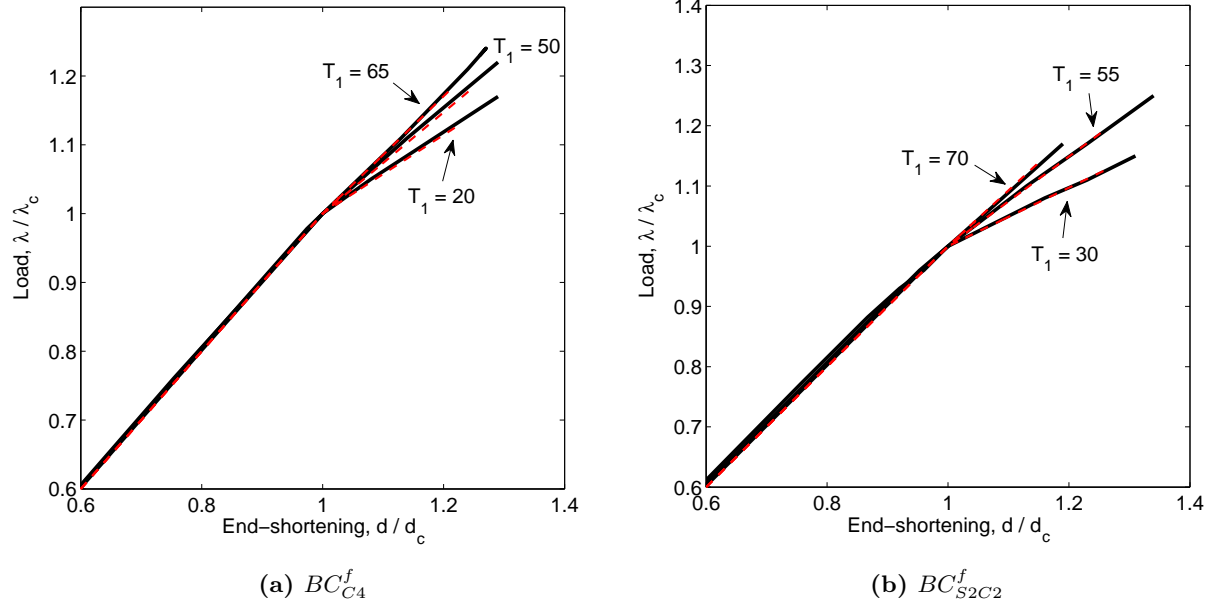

(a) Buckling load versus angle T_1

(b) Equilibrium path for $T_1 = 45°$ and $T_1 = 70°$

Figure 4: Comparison of 2D FE Plate, 2D FE Shell and 3D FEM solutions for boundary condition BC_{C4}^c.

Figure 5: Correlation between DQ shell (dashed) and 3D FEM results (solid) of normalized end-loading λ/λ_c versus normalized end-shortening d/d_c for various edge angles and two boundary conditions.

The aim of the study is to optimize for minimum mass while preventing buckling, first ply failure and heeding the manufacturing constraint of maximum $70°$ shearing angle. Furthermore, the layup is constrained to be balanced and symmetric such that only $[90 \pm \langle T_0^1 | T_1^1 \rangle / \ldots / 90 \pm \langle T_0^n | T_1^n \rangle]_s$ laminates are considered, resulting in a laminate with $N = 4n$ plies. All plies are IM7 8552 with density $\rho = 1571$ kg/m^3, ply thickness 0.125 mm and material properties given previously in Section III.B. The optimization problem may be formulated as follows

$$
\begin{aligned}
\text{Minimize:} \quad & M(\boldsymbol{x}): \quad \rho \int_{-b/2}^{b/2} \int_{-a/2}^{a/2} t(x,y)\mathrm{d}x\mathrm{d}y \\
\text{Variables:} \quad & \boldsymbol{x}: \quad \begin{bmatrix} T_0^1 & \ldots & T_0^n & T_1^1 & \ldots & T_1^n & n \end{bmatrix} \\
\text{Subject to:} \quad & 1) \quad 0° \leq T_s^k \leq 70° \quad (s = 0,1 \text{ and } k = 1\ldots n) \\
& \quad \text{if } \left| T_1^k - T_0^k \right| \leq 2° \rightarrow T_1^k = T_0^k = T \\
& 2) \quad r_k(\boldsymbol{x}): \quad \max_{k\in[1,N]} R_{tw}^k(x_i, y_j) - 1 < 0 \\
& 3) \quad g(\boldsymbol{x}): \quad \lambda_c - 1 > 0.
\end{aligned}
\tag{22}
$$

where $r_k(\boldsymbol{x})$ is the Tsai-Wu failure constraint for each layer k in the prebuckling regime, and $g(\boldsymbol{x})$ is the buckling constraint for the entire laminate. The Tsai-Wu reserve factor R_{tw}^k is calculated at the top and bottom of each ply and at all DQ grid points (x_i, y_j). The former is necessary because membrane and flexural behaviors are coupled even in the prebuckling regime due to the curved nature of the neutral surface. The condition on the magnitude of fiber steering $\left| T_1^k - T_0^k \right| \leq 2°$ is introduced to replace CTS plies with minimal fiber variations with straight fiber plies of unsheared ply thickness $t_0^k = 0.125$ mm. This is important because CTS manufactured straight fiber plies that are not coincident with the steering direction ϕ^k develop thickness build-up along the entire length of the tow. In terms of minimising mass it is thus more efficient to replace plies that do not take advantage of the fiber steering capability with pristine unsheared plies.

The optimization problem is solved using a genetic algorithm (GA) in the commercial software package MATLAB. The crossover probability is chosen to be 0.8 and the children of future generations are created using a weighted average of the parents. The mutation function is a MATLAB adaptive-feasible algorithm that creates random changes in the population individuals with the direction and step length adaptive to the prior successful or unsuccessful generation. The constraint functions $r_k(\boldsymbol{x})$ and $g(\boldsymbol{x})$ are introduced in

the GA using a penalty method, whereby the objective function is re-written as

$$M(\boldsymbol{x}) \cdot \max(1, 1 + r_k(\boldsymbol{x}))^2 \cdot \max(1, 1/\lambda_c)^2. \tag{23}$$

The choice of the penalty exponents needs to be sufficiently large to steer the GA away from unsuccessful designs but not excessively large to prevent the evolution of generations in the vicinity of a marginally unfeasible design. Based on our trial-and-error experience the square law in Eq. (23) provides a good trade-off.

Due to the large number of design variables and the non-convexity of the optimization problem the convergence of the GA is relatively slow and a global minimum is not guaranteed. To improve the convergence rate a hybrid optimization scheme is implemented whereby the GA is used to find the region near an optimum point after only a small number of generations, typically less than 20, and a pattern-search algorithm is then used for a faster and more efficient local search. To prevent entrapment in local minima a variety of random and specific initial seed populations are tested, with the range of individuals in the initial population set to include the whole design space $T_s^k \in [0°, 70°]$ and the population size set to 15-20 times the number of design variables. As shown by Ijsselmuiden et al.[20] the problem of non-convexity may be overcome by using lamination parameters as the design variables. In this case a globally convergent method of moving asymptotes may be used as recently shown by Wu et al.[35] The drawback of this approach is that a second optimization step is required to find realistic layups that approximate the lamination parameter distributions of the optimal results.

Before the GA is initiated, trial-and-error tests are used to determine a feasible number of layers n required to satisfy all failure constraints. The optimization algorithm is then given the freedom to remove and/or add plies to optimize the design. Due to the positive definite and semi-infinite design space n, this initial screening provides an efficient preliminary step for bounding the initial population and reducing computational run-time.

IV.B. Optimization Results

The optimizer is first used to find a baseline straight fiber design QI with mass M_{QI} that complies with the standard aerospace lamination guidelines, i.e. uses only fiber angles $\pm 45°$, $0°$ and $90°$ with at least 10% of each fiber angle in the laminate; prevents blocking of more than four plies; uses $\pm 45°$ on the outside surface for damage tolerance; and is balanced and symmetric. This baseline design is then used to determine the percentage mass reduction of an optimized laminate with mass M_{lam} using

$$\Delta M_{QI}^{lam} = 100 \cdot \frac{M_{QI} - M_{lam}}{M_{QI}}. \tag{24}$$

The optimization results for the square panel are shown in Table 2 and feature the stacking sequence for the baseline design (QI^N), an optimal straight fiber design (SF^N) that does not comply with the aerospace lamination guidelines, and different CTS variable angle tow designs (VAT^N). In each case, the exponent N denotes the total number of layers in the laminate. Furthermore, all fiber angles in the stacking sequences are rounded to the nearest integer to comply with the layup accuracy of the CTS process.[17] Apart from the optimized stacking sequences, Table 2 also shows the lowest eigenvalue λ_c i.e. the lowest load multiplier to induce instability of the fundamental path, the maximum reserve factor R_{tw} throughout the laminate, the maximum axial compressive strain ϵ_x at the design load $P = -250$ kN, the mass of each laminate M and the resulting percentage mass saving calculated from Eq. (24).

The QI^{52} laminate given in Table 2 is one of many possible QI designs, which all differ in their values of λ_c, R_{tw} and ϵ_x. At least 52 plies are required to guarantee that a QI laminate passes all failure criteria which fixes the minimum mass at 638 g but allows for different combinations of the four ply angles $\pm 45°$, $0°$ and $90°$. The optimum straight fiber design SF^{48} eliminates four plies thereby reducing the mass by 7.7% but the maximum compressive strain of -9240 μstrain is beyond the limit magnitude of 4000-5000 μstrain typically employed in the aerospace industry. The fact that λ_c is always closer to unity than R_{tw} suggests that buckling is the critical design criterion for the investigated load case. Therefore, the $[\pm 45]_{12s}$ laminate must be the optimal straight fiber design as it maximizes torsional rigidity and anticlastic curvature resistance, consequently maximizing the buckling performance.[45]

The design with the greatest mass reduction of 31% is a 28-ply hybrid straight fiber-VAT laminate. Furthermore, a second 24-ply design with all laminae in the VAT format and 29.5% mass reduction is also

Table 2: CTS layups for square panel ($a = b = 0.25$ m) optimized for minimum mass with buckling, failure and end-shortening constraints. Percentage mass reduction with respect to QI^{52} laminate.

Laminate	Stacking Sequence	λ_c	R_{tw}	ϵ_x ($\times 10^{-6}$)	M (g)	ΔM_{QI}^{lam} (%)
QI^{52}	$[(\pm45_3/0_2/90_2)_2/\pm45_2/0_2]_s$	1.13	0.30	-2600	638	-
SF^{48}	$[\pm45]_{12s}$	1.00	0.73	-9240	589	7.7
VAT^{24}	$[(90 \pm \langle25|70\rangle)_4/90 \pm \langle27|61\rangle/90 \pm \langle37|24\rangle]_s$	1.00	0.89	-5490	450	29.5
VAT^{28}	$[(90 \pm \langle0|69\rangle)_4/90 \pm \langle0|67\rangle/\pm77/90_2]_s$	1.00	0.70	-6240	440	31.0
$VAT^{28}_{\epsilon5}$	$[90 \pm \langle2|67\rangle/(90 \pm \langle17|65\rangle)_2/90 \pm \langle21|69\rangle/$ $90 \pm \langle38|70\rangle/\pm66/\pm88]_s$	1.03	0.63	-5000	473	25.9
$VAT^{28}_{\epsilon4}$	$[(90 \pm \langle15|64\rangle)_2/90 \pm \langle20|69\rangle/90 \pm \langle40|70\rangle/$ $90 \pm \langle50|67\rangle/90 \pm \langle29|0\rangle/90_2]_s$	1.00	0.44	-4000	502	21.3

Table 3: CTS layups for rectangular panel ($a = 0.75$m, $b = 0.25$m) optimized for minimum mass with buckling, failure and end-shortening constraints. Percentage mass reduction with respect to QI^{52} laminate.

Laminate	Stacking Sequence	λ_c	R_{tw}	ϵ_x ($\times 10^{-6}$)	M (g)	ΔM_{QI}^{lam} (%)
QI^{52}	$[(\pm45_3/0_2/90_2)_2/\pm45_2/0_2]_s$	1.13	0.30	-2600	1915	-
SF^{48}	$[\pm45]_{12s}$	1.00	0.73	-9240	1767	7.7
VAT^{24}	$[(90 \pm \langle20|70\rangle)_4/90 \pm \langle26|59\rangle/90 \pm \langle34|25\rangle]_s$	1.01	0.98	-5960	1309	31.6
VAT^{28}	$[(90 \pm \langle0|69\rangle)_4/90 \pm \langle0|67\rangle/\pm80/90_2]_s$	1.00	0.68	-6190	1321	31.0
$VAT^{28}_{\epsilon5}$	$[90 \pm \langle2|68\rangle/(90 \pm \langle17|64\rangle)_2/90 \pm \langle22|69\rangle/$ $90 \pm \langle38|70\rangle/\pm67/\pm88]_s$	1.03	0.62	-5000	1419	25.9
$VAT^{28}_{\epsilon4}$	$[(90 \pm \langle15|63\rangle)_2/90 \pm \langle19|69\rangle/90 \pm \langle40|70\rangle/$ $90 \pm \langle50|67\rangle/90 \pm \langle23|0\rangle/90_2]_s$	1.01	0.45	-4000	1498	21.8

shown in Table 2. Given that the difference between the VAT^{28} and VAT^{24} design is only 2% the VAT^{24} could be viewed as a superior design if the reduced layup time and material costs are taken into account. In either case, both VAT designs reduce the panel mass by almost a third and cut the ply count in half. Both designs achieve superior performance by using plies with fibers aligned with the loading direction at the panel edges and fibers perpendicular to the load at the panel center. In this manner, the prebuckling stresses are re-directed to the supported areas on the boundary that do not buckle. Furthermore, the curved neutral surface of the VAT laminates also contributes to increasing the buckling load as shown in Section III.B, due to the combined membrane and flexural load carrying capacity of curved panels.

Despite the greater ply count, the VAT^{28} design is lighter than the VAT^{24} design because the former features less thickness build-up associated with the CTS manufacturing process. The VAT^{24} laminate is comprised of purely VAT layers whereas the VAT^{28} laminate includes eight straight fiber plies. This suggests that at some point the marginal increase in buckling performance derived from tow steering is smaller than the marginal increase in associated panel mass. Thus, it becomes more efficient to reduce the number of tow steered plies and improve buckling rigidity by increasing the straight fiber ply count. This coupling of stiffness and mass is not present in AFP laminates and the aim of future work is to compare the performance of respective AFP designs, albeit at the cost of inferior manufacturing quality. A second factor contributing to the lighter VAT^{28} design is that $T_0^k = 0°$ for all CTS layers such that the central portion of the panel remains at the unsheared laminate thickness. However, the VAT^{24} design features $T_0^k \geq 25°$ for all layers such that a greater portion of the panel has an increased ply thickness due to tow shearing.

The central angle of $T_0^k \geq 25°$ is required because of the competing buckling and static failure constraints imposed on the design. In the VAT^{28} design these two functions are split between different portions of the stacking sequence. The outer VAT layers predominantly provide buckling rigidity, strength in the axial

x-direction at the panel edges and strength in the lateral y-direction at the panel center. However, this leaves the panel susceptible to axial and shear failure at the panel center and matrix cracking at the panel edges, and these are mitigated by the $\pm 77°$ angle plies and $90°$ plies. In the VAT[24] design the buckling and strength functions are combined in all variable stiffness plies. The 20 outside plies provide sufficient buckling rigidity by redirecting loads to the panel edges, while also introducing axial x-direction, lateral y-direction and shear strength at the panel center due to the local fiber angle of $\sim \pm 65°$. Finally, the four central plies $[90 \pm \langle 37|24 \rangle]_s$ provide the required lateral and shear strength at the panel edges, transitioning to further axial and shear support at the panel center.

Due to the combined functionality within plies the VAT[24] laminate reduces the number of plies and also increases the axial rigidity. The maximum compressive strain in the VAT[24] laminate is 12% less than in the VAT[28] laminate and at -5490 μstrain almost within the 4000-5000 μstrain magnitude range deemed safe in the aerospace industry. To comply with this design guideline the optimization scheme is altered to find feasible designs at the lower and upper ends of this range. Thus, an additional constraint function $e(\boldsymbol{x})$ is added

$$e(\boldsymbol{x}): \quad |\epsilon_x| - |\epsilon_x^c| < 0. \tag{25}$$

where ϵ_x^c is the applied strain constraint such that the objective function is re-written as

$$M(\boldsymbol{x}) \cdot \max(1, 1 + r_k(\boldsymbol{x}))^2 \cdot \max(1, 1/\lambda_c)^2 \cdot \max(1, |\epsilon_x| / |\epsilon_x^c|)^2. \tag{26}$$

The optimized designs at the lower and upper ends of the strain range are denoted by $\text{VAT}_{\epsilon 4}^{28}$ and $\text{VAT}_{\epsilon 5}^{28}$ in Table 2, respectively. In both cases a 28-ply design results in the minimum mass layup. Trial-and-error studies show that for a 24-ply design the maximum compressive strain magnitude cannot be reduced to below 5000 μstrain while also satisfying the buckling load constraint. This occurs because the buckling performance is driven by load re-distribution towards supported edges whereas the axial strain depends on the average axial stiffness over the panel planform. Compared to straight fiber laminates, variable stiffness designs can locally increase axial stiffness but at the same time reduce the average axial stiffness of the panel. Thus, there exists a trade-off between increasing axial stiffness locally for enhanced buckling performance, and maintaining high axial stiffness globally for benign axial strains.[23] Under these circumstances, the greater design freedom of the 28-ply over the 24-ply laminate allows a more efficient compromise to be reached. As mass is removed from future aerospace structures, the susceptibility to instability naturally increases and the need for local stiffness tailoring to increase the instability threshold gains importance. To realize these optimized structures design guidelines may need to adapt to allow for structures with greater strains.

The results in Table 2 show that the panel mass increases by 7.5% between VAT[28] and $\text{VAT}_{\epsilon 5}^{28}$, i.e. when the compressive axial strain constraint of -5000 μstrain is enforced. There is a further 6.1% increase between $\text{VAT}_{\epsilon 5}^{28}$ and $\text{VAT}_{\epsilon 4}^{28}$ when the threshold is reduced to -4000 μstrain. Even though the $\text{VAT}_{\epsilon 4}^{28}$ laminate betters the baseline QI design by a fifth, the strain constraint significantly impacts the mass savings that can be achieved. Considering that the maximum Tsai-Wu reserve factor is 0.44 for the $\text{VAT}_{\epsilon 4}^{28}$ design such that the laminate is only at half its loading capacity, the 4000-5000 μstrain range appears to be overly conservative.

As discussed previously, this conservativeness arises due to two distinct requirements of local and global stiffness tailoring that influence the buckling performance and axial strain, respectively. In fact, this tradeoff is apparent in the stacking sequence of the $\text{VAT}_{\epsilon 4}^{28}$ design. Here the edge angle $T_1^k \approx 70°$ in the outer layers redistributes loads to the edges. However, the central angle T_0^k has increased from $0°$ for the VAT[28] laminate to $15° - 50°$ in the $\text{VAT}_{\epsilon 4}^{28}$ design. This is equivalent to changing the fiber direction from $90°$ in the global xy-coordinate system to $40° - 75°$, thereby aligning more fibers with the loading direction and imparting increased axial stiffness. Secondly, the $\pm 77°$ plies, which provide lateral y-direction strength at the panel edges in the VAT[28] laminate, are altered into variable stiffness plies $[90 \pm \langle 29|0 \rangle]$ in the $\text{VAT}_{\epsilon 4}^{28}$ laminate. The $\pm 61°$ fiber directions at the panel center now provide increased axial stiffness whereas the $90°$ at the panel edges retain the lateral strength.

Similarly, the optimization results for a rectangular panel ($a = 0.75$ m, $b = 0.25$ m) are shown in Table 3. The optimized stacking sequences follow the same general trends as the square panel ($a = b = 0.25$ m) stacking sequences discussed above. The difference in respective ply angles between the square and rectangular panels is at most a few degrees resulting in the same overall percentage mass savings. The largest change occurs for the VAT[24] laminate which now supercedes the VAT[28] laminate as the best design with 31.6% mass savings. Compared to the VAT[24] layup for the square panel the relative reductions in mass occur because the central angle T_0^k for the outer eight plies has been reduced from $25°$ to $20°$. In these plies the tows towards the central portion of the panel are sheared less resulting in thinner plies and

consequently reduced mass. On the other hand, this degrades axial stiffness such that the axial compressive strain increases in magnitude by 8.6%. Finally, with $\lambda_c = 1.01$ and $R_{tw} = 0.98$ the laminate is close to violating both failure criteria on buckling and static strength simultaneously suggesting that the design is close to optimal.

Due to the curvature of the neutral surface, the postbuckling behavior of a CTS panel may be governed by a falling equilibrium path. This quality, which is characteristic of curved panels and cylindrical shells, means the structure may lose all its load carrying capability at the point of buckling and be highly sensitive to prebuckling imperfections that may drastically reduce the buckling load. Thus, the initial postbuckling path of the optimized laminates in Tables 2 and 3 need to be investigated in detail.

IV.C.   Postbuckling Stability

As outlined in Section II.B the initial postbuckling behavior of the optimized panels is investigated using Koiter's perturbation approach. Here the buckling mode $\boldsymbol{u}_1$ and prebuckling load resultants $\boldsymbol{N}_0$ are used to solve the initial postbuckling problem given by Eq. (30) in the Appendix. In essence, the buckling mode $\boldsymbol{u}_1$ is used to perturb the equilibrium path about the point of buckling. In this manner the quadratic postbuckling mode $\boldsymbol{u}_2$ corresponding to a certain buckling mode $\boldsymbol{u}_1$ is ascertained and the postbuckling equilibrium path written in terms of a power series of the perturbation parameter p (see Eq. (13)). The stability of this postbuckling path close to the bifurcation point is studied using the path coefficients λ_1 and λ_2 defined in Eq. (15) which indicate whether the load-displacement curve past the bifurcation point is rising or falling. The first two buckling loads in a curved panel are often coincident or closely spaced such that both postbuckling solutions need to be investigated to adequately assess postbuckling stability. This is achieved by solving for the respective quadratic postbuckling mode $\boldsymbol{u}_2$ of both the first and second buckling modes $\boldsymbol{u}_1$.

Table 4 shows the critical eigenvalues λ_c, the normalized path coefficients $|\lambda_1/\lambda_c|$ and λ_2/λ_c, and the linearized postbuckling stiffness K_{pb} of a stable path for each of the square panels in Table 2. A non-zero value of $|\lambda_1/\lambda_c|$ indicates asymmetry about the bifurcation point which is characteristic of curved panels. A negative value of λ_2/λ_c indicates a falling load-displacement path and means the postbuckling mode is unstable. The results show that nearly all optimized square CTS designs have stable postbuckling paths for the first two buckling modes with the exception of the VAT[28] laminate, which has been underlined in Table 4. The bifurcation behavior may be visualized with the help of Figure 6 which shows a plot of out-of-plane buckling displacement versus applied load for the idealized VAT[28] laminate. As the load is increased from zero, the structure is initially stable on the prebuckling path with zero out-of-plane buckling displacement w_1. At $\lambda_c = \lambda_{c_1}$ the panel bifurcates into the unstable first mode which is characterized by a falling load-displacement curve. The load-displacement curve of the second buckling mode is rising but is induced on the fundamental path at loads 4% greater than the first mode. In reality, it is not clear how the structure behaves upon bifurcating and the behavior is highly dependent on the initial configuration. For example, given that the second eigenvalue is relatively close to the first, an initial imperfection resembling the second mode may coax the structure to bifurcate into this configuration. However, such a behavior is not guaranteed by any means making the panel highly sensitive to the initial configuration and hence, not suitable for robust design. In light of these findings an additional constraint condition on the path parameter λ_2 of the first two buckling modes should be included in the optimization study in order to safeguard against unstable postbuckling behavior and this will be the topic of future work.

The normalized load versus end-shortening curves of the first buckling mode near the bifurcation point of the QI[52], VAT[24], VAT[28], VAT$_{\epsilon5}^{28}$ and VAT$_{\epsilon4}^{28}$ laminates for the square panel are shown in Figure 7a. The reversing postbuckling path for the VAT[28] laminate supports the observations made previously that the panel is incapable of carrying load upon bifurcation into the first mode and collapses unless a mode jump into an adjacent shape occurs. Due to a non-zero asymmetry parameter λ_1 the other three CTS panels VAT[24], VAT$_{\epsilon5}^{28}$ and VAT$_{\epsilon4}^{28}$ are not invariant to the direction of buckling such that the equilibrium path branches into two solutions. In each case buckling in one direction leads to a smooth bifurcation onto the lower postbuckling path, whereas buckling in the opposite direction results in a load drop under controlled end-shortening or a sudden reduction in end-shortening under dead load. However, in both cases these jumps in end-shortening or load are less than 0.5% and can be considered as harmless to the structure. Figure 7a and the K_{pb} values in Table 4 also show that the stable CTS panels significantly improve the postbuckling stiffness compared to the QI[52] laminate. Considering this, the possibility arises to design variable stiffness panels with benign strains in the postbuckling regime which, by relaxing the buckling constraint, could lead

Table 4: Initial postbuckling path coefficients of optimized CTS layups for square panel ($a = b = 0.25$m). Negative λ_2/λ_c indicate unstable postbuckling equilibrium branches and these are underlined.

Laminate	Mode	λ_c	$|\lambda_1/\lambda_c|$	λ_2/λ_c	K_{pb}
QI^{52}	1	1.13	0	2.61×10^{-1}	0.48
SF^{48}	1	1.00	0	7.69×10^{-2}	0.50
VAT^{24}	1	1.00	2.29×10^{-2}	4.76×10^{-2}	0.76
	2	1.18	6.86×10^{-5}	9.02×10^{-2}	0.72
VAT^{28}	1	1.00	1.15×10^{-5}	$\underline{-7.54\times10^{-1}}$	-
	2	1.04	4.72×10^{-2}	2.35×10^{-1}	0.87
$\text{VAT}^{28}_{\epsilon5}$	1	1.03	1.70×10^{-3}	7.38×10^{-2}	0.74
	2	1.07	8.32×10^{-5}	1.51×10^{-1}	0.71
$\text{VAT}^{28}_{\epsilon4}$	1	1.00	9.34×10^{-3}	8.71×10^{-2}	0.70
	2	1.11	4.84×10^{-5}	1.78×10^{-1}	0.64

Table 5: Initial postbuckling path coefficients of optimized CTS layups for rectangular panel ($a = 0.75$m, $b = 0.25$m).

| Laminate	Mode	λ_c	$|\lambda_1/\lambda_c|$	λ_2/λ_c	K_{pb}
QI^{52}	1	1.13	0	2.61×10^{-1}	0.48
SF^{48}	1	1.00	0	7.68×10^{-2}	0.50
VAT^{24}	1	1.01	4.25×10^{-2}	5.92×10^{-2}	0.83
	2	1.02	2.02×10^{-3}	2.48×10^{-2}	0.65
VAT^{28}	1	1.00	4.78×10^{-2}	8.40×10^{-2}	0.74
	2	1.01	9.75×10^{-6}	1.96×10^{-2}	0.33
$\text{VAT}^{28}_{\epsilon5}$	1	1.03	4.32×10^{-2}	8.37×10^{-2}	0.72
	2	1.06	9.19×10^{-5}	1.30×10^{-1}	0.71
$\text{VAT}^{28}_{\epsilon4}$	1	1.01	2.07×10^{-4}	7.08×10^{-2}	0.58
	2	1.02	3.35×10^{-2}	9.87×10^{-2}	0.66

to further mass reductions.

Similarly, Table 5 summarizes the path coefficients for each of the rectangular panels in Table 3. In this case all variable stiffness laminates have two stable buckling modes. The load-displacement curves for the first mode shape of laminates QI^{52}, VAT^{24}, $\text{VAT}^{28}_{\epsilon5}$ and $\text{VAT}^{28}_{\epsilon4}$ are shown in Figure 7b. The plot shows that the two postbuckling branches for laminate $\text{VAT}^{28}_{\epsilon4}$ are coincident making the panel invariant to the direction of buckling. This behavior occurs because the value of $|\lambda_1/\lambda_c| = 2.07 \times 10^{-4}$ for the first buckling mode, as shown in Table 5, is two orders of magnitude less than $|\lambda_2/\lambda_c| = 7.08 \times 10^{-2}$. For the VAT^{24} and $\text{VAT}^{28}_{\epsilon5}$ laminates $|\lambda_1/\lambda_c|$ and $|\lambda_2/\lambda_c|$ are of the same order of magnitude such that two distinct postbuckling branches exist. The presence of this asymmetric bifurcation means that the CTS panels are sensitive to imperfections as shown by the dotted curve in Figure 7b. In the presence of initial imperfections the idealized buckling load is not reached and the panel bifurcates at reduced load which is proportional to the magnitude of the load drop on the idealized postbuckling path. For the panels in Figure 7b the consequences of this imperfection sensitivity are benign as the load drop is at most 1% and the postbuckling paths of the CTS panels rise faster than that of the straight fiber QI^{52} laminate.

V.   Conclusions

The aim of this study is to find a minimum-mass design of a typical aircraft wing panel under end-compression using advanced composite materials that allow the fibers to vary spatially over the planform of the panel. These variable angle tow (VAT) composites may be manufactured to pre-preg like quality using a manufacturing technique known as Continuous Tow Shearing (CTS). One added complexity of the
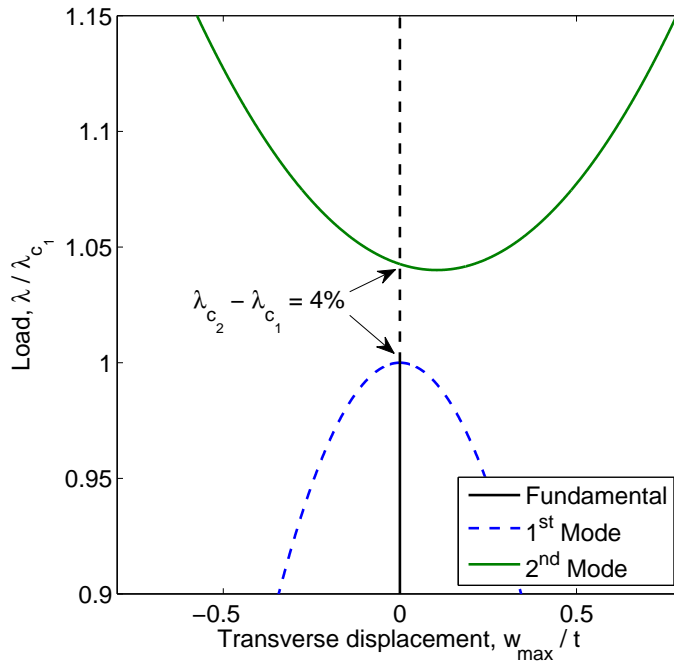
Figure 6: Fundamental and first two postbuckling paths for the square VAT[28] CTS panel. The plot of load versus transverse displacement shows stable and unstable paths as solid and dashed curves, respectively.

(a) Square $a = b = 0.25$ m

(b) Rectangular $a = 0.75$ m, $b = 0.25$ m
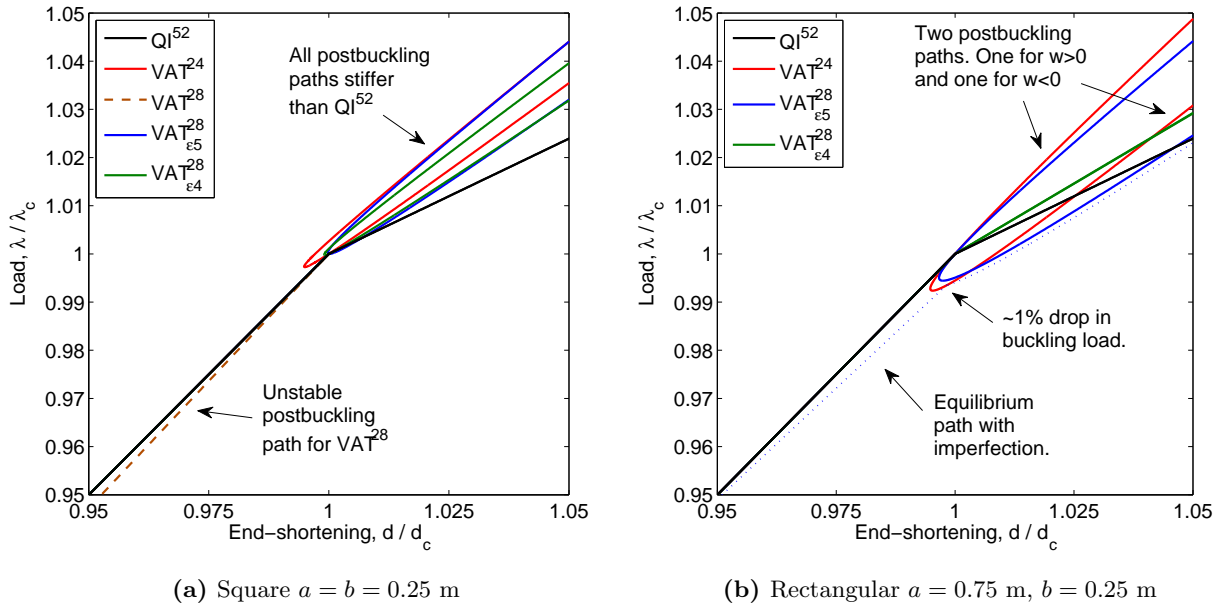
Figure 7: Fundamental and initial postbuckling paths for different optimized CTS layups. The annotated layups for the square and rectangular panels correspond to the results in Table 2 and Table 3, respectively. Unstable equilibrium paths are denoted by dashed curves. The equilirbium path for the rectangular VAT$_{\epsilon 5}^{28}$ laminate with initial imperfections is shown by a dotted curve.

CTS process is that the fiber steering angle and the thickness of the steered tow are coupled by a secant law, which results in an asymmetric thickness profile when the panel is cured on a tool plate. Compressing this three-dimensional profile onto an equivalent single layer results in a curved reference surface whose geometric effects on the structural behavior need to be taken account of. The results of this study show that the prebuckling, buckling and postbuckling behavior of the variable stiffness panels can be captured adequately using the equilibrium equations of a shallow cylindrical shell with variable radius of curvature.

Coupling this analytical model with a genetic algorithm subject to pre-defined manufacturing, static failure and buckling load constraints results in an optimized VAT laminate that reduces the mass of both square and rectangular aircraft panels by 31% compared to a baseline straight fiber design. When an additional maximum compressive strain constraint of -4000 μstrain is enforced the potential mass savings reduce to 21.5%. It is shown that the optimization of the fiber orientations is driven by two distinct requirements of local and global stiffness tailoring that influence the buckling performance and static strength, respectively. Thus, a compromise needs to be reached between locally re-distributing loads to supported areas for enhanced buckling performance and maintaining high average stiffness over the panel planform for benign axial strains. It is also observed that one of the optimized designs suffers from unstable postbuckling behavior. Thus, it is imperative to incorporate an additional constraint condition in the optimization framework in order to safeguard against unstable postbuckling behavior.

In light of current fuel and efficiency regulations aerospace structures of the future will need to become thinner and more lightweight. Under these circumstances, the susceptibility to instability increases and the role of local stiffness may play a more prominent role in the design of aerospace structures. The present work shows that variable stiffness laminates can be designed to exhibit stiffer postbuckling behavior than their straight fiber counterparts. Considering this, future aircraft structures could achieve greater levels of efficiency if these nonlinearities in structural behavior are exploited in a controlled and safe manner.

Appendix

All functional fields are expanded in terms of the perturbation parameter p as expressed in Eq. (13). In the present analysis only the initial postbuckling behavior is of interest such that the expansion includes terms up to the second order of p. Thus, the membrane forces and bending moments are written as

$$\boldsymbol{N} = \begin{pmatrix} N_x & N_y & N_{xy} \end{pmatrix}^T = \boldsymbol{N}_0 + p\boldsymbol{N}_1 + p^2\boldsymbol{N}_2 \tag{27a}$$

$$\boldsymbol{M} = \begin{pmatrix} M_x & M_y & M_{xy} \end{pmatrix}^T = \boldsymbol{M}_0 + p\boldsymbol{M}_1 + p^2\boldsymbol{M}_2. \tag{27b}$$

Substituting the perturbed displacement field Eq. (13) into the perturbed stress resultants Eq. (27) and further into the governing equations (10) we write

Prebuckling Equations

$$\delta u_0 : N_{x0,x} + \frac{1}{R}M_{y0,x} + \left(\frac{N_{xy0}}{A_2}\right)_{,y} - \left(\frac{M_{xy0}}{RA_2}\right)_{,y} = 0 \tag{28a}$$

$$\delta v_0 : \left(\frac{N_{y0}}{A_2}\right)_{,y} + \left(\frac{M_{y0}}{RA_2}\right)_{,y} + N_{xy0,x} + \frac{1}{R}M_{xy0,x} = 0 \tag{28b}$$

$$\delta w_0 : M_{x0,xx} + 2\left(\frac{M_{xy0,x}}{A_2}\right)_{,y} + \left(\frac{M_{y0}}{(A_2)^2}\right)_{,yy} - \frac{N_{y0}}{R} + \left(M_{y0}\frac{A_{2,y}}{(A_2)^3}\right)_{,y} = 0 \tag{28c}$$

Buckling Equations

$$\delta u_1 : N_{x1,x} + \frac{1}{R}M_{y1,x} + \left(\frac{N_{xy1}}{A_2}\right)_{,y} - \left(\frac{M_{xy1}}{RA_2}\right)_{,y} = 0 \tag{29a}$$

$$\delta v_1 : \left(\frac{N_{y1}}{A_2}\right)_{,y} + \left(\frac{M_{y1}}{RA_2}\right)_{,y} + N_{xy1,x} + \frac{1}{R}M_{xy1,x} = 0 \tag{29b}$$

$$\delta w_1 : M_{x1,xx} + 2\left(\frac{M_{xy1,x}}{A_2}\right)_{,y} + \left(\frac{M_{y1}}{(A_2)^2}\right)_{,yy} - \frac{N_{y1}}{R} + \left(M_{y1}\frac{A_{2,y}}{(A_2)^3}\right)_{,y} + (N_{x0}w_{1,x})_{,x} + \frac{1}{A_2}(N_{xy0}w_{1,y})_{,x} +$$

$$\left(\frac{N_{xy0}}{A_2} w_{1,x} \right)_{,y} + \left(\frac{N_{y0}}{(A_2)^2} w_{1,y} \right)_{,y} = 0 \tag{29c}$$

Initial Postbuckling Equations

$$\delta u_2 : N_{x2,x} + \frac{1}{R} M_{y2,x} + \left(\frac{N_{xy2}}{A_2} \right)_{,y} - \left(\frac{M_{xy2}}{RA_2} \right)_{,y} = 0 \tag{30a}$$

$$\delta v_2 : \left(\frac{N_{y2}}{A_2} \right)_{,y} + \left(\frac{M_{y2}}{RA_2} \right)_{,y} + N_{xy2,x} + \frac{1}{R} M_{xy2,x} = 0 \tag{30b}$$

$$\delta w_2 : M_{x2,xx} + 2 \left(\frac{M_{xy2,x}}{A_2} \right)_{,y} + \left(\frac{M_{y2}}{(A_2)^2} \right)_{,yy} - \frac{N_{y2}}{R} + \left(M_{y2} \frac{A_{2,y}}{(A_2)^3} \right)_{,y} + (N_{x0} w_{2,x} + N_{x1} w_{1,x})_{,x} +$$

$$\frac{1}{A_2} (N_{xy0} w_{2,y} + N_{xy1} w_{1,y})_{,x} + \left(\frac{N_{xy0} w_{2,x} + N_{xy1} w_{1,x}}{A_2} \right)_{,y} + \left(\frac{N_{y0} w_{2,y} + N_{y1} w_{1,y}}{(A_2)^2} \right)_{,y} = 0. \tag{30c}$$

In addition the integral expression,

$$\int \int \left[(N_{x0} w_{2,x} + N_{xy0} w_{2,y}) w_{1,x} + (N_{y0} w_{2,y} + N_{xy0} w_{2,x}) w_{1,y} \right] \mathrm{d}x \mathrm{d}y = 0 \tag{31}$$

should be satisfied in order to enforce the orthogonality of the linear and quadratic buckling displacement fields u_1 and u_2. Details for solving the above equations in MATLAB using DQM are presented by White et al.[37]

Acknowledgments

References

[1] Cooper, A. A. G., *Trajectorial fiber reinforcement of composite structures*, Ph.D. thesis, Department of Mechanical and Aerospace Engineering, Washington University, 1972.

[2] Hyer, M. W. and Lee, H. H., "The use of curvilinear fiber format to improve buckling resistance of composite plates with central circular holes," *Composite Structures*, Vol. 18, 1991, pp. 239–261.

[3] Hyer, M. W. and Charette, R. F., "The use of curvilinear fiber format in composite structure design," *AIAA J.*, Vol. 29, No. 6, 1991, pp. 1011–1015.

[4] Gurdal, Z. and Olmedo, R., "In-plane response of laminates with spatially varying fiber orientations: variable stiffness concept," *AIAA J.*, Vol. 31, No. 4, 1993, pp. 751–758.

[5] Gurdal, Z., Tatting, B. F., and Wu, C. K., "Variable stiffness composite panels: effects of stiffness variation on the in-plane and buckling response," *Composites: Part A*, Vol. 39, 2008, pp. 911–922.

[6] Wu, Z., Weaver, P. M., Raju, G., and Kim, B. C., "Buckling analysis and optimisation of variable angle tow composite plates," *Thin-Walled Structures*, Vol. 60, 2012, pp. 163–172.

[7] Raju, G., Z., W., C., K. B., and M., W. P., "Prebuckling and buckling analysis of variable angle tow plates with general boundary conditions," *Composite Structures*, Vol. 94, No. 9, 2012, pp. 2961–2970.

[8] van den Brink, W. M., Vankan, W. J., and Maas, R., "Buckling optimized variable stiffness laminates for a composite fuselage window section," 2012.

[9] Alhajahmad, A., Abdalla, M. M., and Gurdal, Z., "Optimal design of tow-placed fuselage panels for maximum strength with buckling considerations," *Journal of Aircraft*, Vol. 47, No. 3, 2010, pp. 775–782.

[10] Coburn, B. H., Wu, Z., and Weaver, P. M., "Buckling analysis of stiffened variable angle tow panels," *Composite Structures*, Vol. 111, 2014, pp. 259–270.

[11] Wu, Z., Gangadharan, R., and Weaver, P. M., "Postbuckling analysis of variable angle tow composite plates," *International Journal of Solids and Structures*, Vol. 50, 2013, pp. 1770–1780.

[12] Wu, Z., Weaver, P. M., and Gangadharan, R., "Postbuckling optimisation of variable angle tow composite plates," *Composite Structures*, Vol. 103, 2013, pp. 34–42.

[13] Blom, A. W., *Structural performance of fiberplaced variable-stiffness composite conical and cylindrical shells*, Ph.D. thesis, University of Delft, 2010.

[14] Beakou, A., Cano, M., Le Cam, J.-B., and Verney, V., "Modelling slit tape buckling during automated prepreg manufacturing: A local approach," *Composite Structures*, Vol. 93, 2011, pp. 2628–2635.

[15]Fayazbakhsh, K., Nik, M. A., Pasini, D., and Lessard, L., "Defect layer method to capture effect of gaps and overlaps in variable stiffness laminates made by Automated Fiber Placement Kazem," *Composite Structures*, Vol. 97, 2013, pp. 245–251.

[16]Kim, B. C., Potter, K., and Weaver, P. M., "Continuous tow shearing for manufacturing variable angle tow composites," *Composites: Part A*, Vol. 43, No. 8, 2012, pp. 1347–1356.

[17]Kim, B. C., Weaver, P. M., and Potter, K., "Manufacturing characteristics of the continuous tow shearing method for manufacturing of variable angle tow composites," *Composites: Part A*, Vol. 61, No. 8, 2014, pp. 141–151.

[18]Groh, R. M. J. and Weaver, P. M., "Buckling analysis of variable angle tow, variable thickness panels with transverse shear effects," *Composite Structures*, Vol. 107, 2014, pp. 482–493.

[19]Setoodeh, S., Abdalla, M. M., Ijsselmuiden, S. T., and Gurdal, Z., "Design of variable stiffness composite panels for maximum buckling load," *Composite Structures*, Vol. 87, 2008, pp. 109–117.

[20]Ijsselmuiden, S. T., Abdalla, M. M., and Gurdal, Z., "Optimization of Variable-Stiffness Panels for Maximum Buckling Load Using Lamination Parameters," *Journal of Aircraft*, Vol. 48, No. 1, 2010, pp. 134–143.

[21]van Campen, J. M. J. F., Kassapoglou, C., and Gurdal, Z., "Generating realistic laminate fiber angle distributions for optimal variable stiffness laminates," *Composites: Part B*, Vol. 43, 2012, pp. 354–360.

[22]Nik, M. A., Fayazbakhsh, K., Pasini, D., and Lessard, L., "Surrogate-based multi-objective optimization of a composite laminate with curvilinear fibres," *Composite Structures*, Vol. 94, 2012, pp. 2306–2313.

[23]Nik, M. A., Fayazbakhsh, K., Pasini, D., and Lessard, L., "Optimization of variable stiffness composites with embedded defects induced by Automated Fiber Placement," *Composite Structures*, Vol. 107, 2014, pp. 160–166.

[24]Liu, W. and Butler, R., "Buckling optimization of Variable-Angle-Tow Panels using the infinite-strip method," *AIAA Journal*, Vol. 51, 2013, pp. 1442–1449.

[25]Amabili, M., *Nonlinear Vibrations and Stability of Shells and Plates*, Cambridge University Press, New York, NY, USA, 2008.

[26]Von Kármán, T., Sechler, E. E., and Donnell, L. H., "The strength of thin plates in compression," *A.S.M.E. Transactions*, Vol. 52, No. 2, 1932, pp. 53–57.

[27]Marguerre, K. and Trefftz, E., "Ueber die Tragfahigkeit eines laengsbelasteten Plattenstreifens anch Ueberschreiten der Beullast," *Z.f.a.M.M.*, Vol. 17, No. 2, 1937, pp. 85–100.

[28]Kromm, A. and Marguerre, K., "Behaviour of a plate-Strip under shear and compressive stresses beyond the buckling limit," Technical Memorandums 870, National Advisory Committee for Aeronautics, 1938.

[29]Levy, S., "Bending of rectangular plates with large deflections," Technical Notes 737, National Advisory Committee for Aeronautics, 1942.

[30]Hu, P. C., Lundquist, E. E., and Batdorf, S. B., "Effect of small deviations from flatness on effective width and buckling of plates in compression," Technical Notes 1124, National Advisory Committee for Aeronautics, 1946.

[31]Rahman, T., *A perturbation approach for geometrically nonlinear structural analysis using a general purpose finite element code*, Ph.D. thesis, University of Delft, 2009.

[32]Koiter, W. T., *De meedragende breedte bij groote overschrijding der knikspanning voor verschillende inklemming der plaatrandenls*, Ph.D. thesis, Nationaal lucht- en ruimtevaartlaboratorium, Amsterdam, The Netherlands, 1943.

[33]Stein, M., "Loads and deformations of buckled rectangular plates," Technical Report R-40, National Aeronautics and Space Administration, 1959.

[34]Chandra, R. and Raju, B. B., "Postbuckling analysis of rectangular orthotropic plates," *Int. J. Mech. Sci.*, Vol. 15, 1973, pp. 81–97.

[35]Wu, Z., Raju, G., White, S., and Weaver, P. M., "Optimal Design of Postbuckling Behaviour of Laminated Composite Plates using Lamination Parameters," *Proceedings of the 55th AIAA/ASMe/ASCE/AHS/SC Structures, Structural Dynamics, and Materials Conference*, Maryland, USA, 2014.

[36]Casciaro, R., Garcea, G., Attanasio, G., and Giordano, F., "Perturbation approach to elastic post-buckling analysis," *Computers & Structures*, Vol. 66, 1998, pp. 585–595.

[37]White, S., Raju, G., and Weaver, P. M., "Initial post-buckling of variable-stiffness curved panels," *Journal of the Mechanics and Physics of Solids*, 2014.

[38]Liang, K., *A Koiter-Newton arclength method for buckling-sensitive structures*, Ph.D. thesis, University of Delft, 2013.

[39]Budiansky, B., "Theory of buckling and post-buckling behavior of elastic structures," *Advances in Applied Mechanics*, Vol. 14, 1974, pp. 1–65.

[40]Bellman, R., Kashef, G., and Casti, J., "Differential quadrature: a technique for the rapid solution of nonlinear partial differential equations," *J. Comput. Phys.*, Vol. 10, 1972, pp. 40–52.

[41]Shu, C., *Differential Quadrature and its Application in Engineering*, Springer Verlag, 2000.

[42]Tsai, S. W. and Wu, E. M., "A general theory of strength for anisotropic materials," *Journal of Composite Materials*, Vol. 5, 1971, pp. 58–80.

[43]Cui, W. C., Wisnom, M. R., and Jones, M., "A comparison o failure criteria to predict delamination of unidirectional glass/epoxy specimens waisted through the thickness," *Composites*, Vol. 23, 1971, pp. 158–166.

[44]Soden, P. D., Kaddour, A. S., and Hinton, M. J., "Recommendations for designers and researchers resulting from the world-wide failure exercise," *Composites Science and Technology*, Vol. 64, 2004, pp. 589–604.

[45]Weaver, P. M., "Anisotropic elastic tailoring in laminated composite plates and shells," *Computational and Experimental Methods in Structures: Volume 1*, edited by B. Falzon and M. H. Aliabadi, Imperial College Press, London, 2008, pp. 177–224.